Article

Two Birds with One Stone: Ammonium-Induced Carbon Nanotube Structure and Low-Crystalline Cobalt Nanoparticles Enabling High Performance of Lithium-Sulfur Batteries

Qi Tan [1], Hongliang Liu [2], Guozhu Liang [2], Kaigui Jiang [2], Hangxuan Xie [3], Weijie Si [4], Jiajv Lin [4,*] and Xiongwu Kang [4,*]

1   Guangdong Electric Power Development Co., Ltd., Guangzhou 510080, China
2   Guangdong Zhuhai Jinwan Power Co., Ltd., Zhuhai 519000, China
3   China Southern Power Grid Technology Co., Ltd., Guangzhou 510080, China
4   New Energy Research Institute, School of Environment and Energy, South China University of Technology, Guangzhou 510006, China
*   Correspondence: linjiaju@dg.gd.csg.cn (J.L.); esxkang@scut.edu.cn (X.K.)

Abstract: The electrochemical performance of lithium–sulfur batteries (LiSBs) has been hampered by the slow redox kinetics and shuttle effect of lithium polysulfides (LiPSs), which require the rational design and synthesis of highly active electrocatalysts towards this reaction. Herein, worm-like N-doped porous carbon nanotube-supported low-crystalline Co nanoparticles (a-Co-NC@C) were derived from binary Zn–Co ZIF via a two-step thermal annealing method. Initial thermal annealing 950 °C in Ar + H_2 atmosphere results in the carbonization of binary Zn–Co ZIF and the formation of high crystalline Co nanoparticles. Thermal annealing in ammonia atmosphere at 350 °C not only results in the reduced crystallinity of cobalt nanoparticles; it also promotes the growth of highly graphitized and heavily N-doped intertwined carbon nanotubes. The enlarged porous carbon nanotube structure offers accommodation for sulfur content, while the doped carbon and Co nanoparticles with reduced crystallinity facilitate the redox kinetics of LiPSs, improving the cycling stability, rate performance and capacity of LiSBs batteries. As a result, the a-Co-NC@C cathode displays a specific capacity of 559 mAh g^{-1} after 500 cycles at 1 C, and a specific capacity of 572 mAh g^{-1} at 3 C. It delivers a specific capacity of 579 mAh g^{-1} at high sulfur loading of a 2.55 mg cm^{-2} at 1 C after 400 cycles. This work highlights the importance of phase engineering of carbon matrix and transition metal nanoparticles in electrochemical performance of Li-S batteries.

Keywords: porous carbon nanotube; low crystalline; cobalt nanoparticles; promoted redox kinetics; Li–S batteries

1. Introduction

As the demand for energy storage continues to grow, commercially mature and widely used lithium-ion batteries, which are close to their theoretical energy density, are no longer able to meet society's energy storage needs [1,2]. In particular, the emergence of electric vehicles requires batteries with high energy density, small size and high safety performance [3–6]. Among the many secondary batteries, lithium–sulfur (Li–S) batteries have become a hot research topic in recent decades due to their high theoretical specific capacity and energy density, as well as their low environmental contamination [7–9]. However, the practical application of Li–S batteries is constrained by their own disadvantages [10–12], such as the non-conductive nature of the sulfur itself, the dissolution and "shuttle effect" of lithium polysulfide (Li_2PSs) and the slow redox kinetics of polysulfide [13–15].

Extensive efforts have been made to improve the charge capacity, cycling and rate performance of Li–S batteries. Porous carbon materials have been used as the sulfur host, which can not only improve the electrical conductivity of the cathode but also suppress the

dissolution of LiPSs. For instance, the coral-like N-doped multilayer porous carbon [16], when utilized as the cathode of Li–S batteries, delivers an initial discharge capacity of 1617 mAh g^{-1} at 0.1 C and a capacity decay rate of only 0.05% per cycle up to 500 cycles at 0.5 C. N-doped porous carbon microspheres (NPCSM), derived from microalgae [17], greatly inhibit the diffusion of PSs by strong physical and chemical adsorption and exhibit a specific capacity of 1030.7 mAh g^{-1} at a current density of 0.1 A g^{-1} as a cathode of Li–S batteries and a capacity of 692.3 mAh g^{-1} at a high current density of 5 A g^{-1}.

Due to the weak interaction between the non-polar carbon material and PSs, the electrochemical performance of Li–S batteries is still unsatisfactory. Therefore, metal contents are introduced into the porous carbon materials, which behave as electrocatalyst towards redox reaction of PSs. Metal organic frameworks (MOF) have been widely used to prepare porous carbon as the sulfur host in Li–S batteries due to their tunable structural composition, rich void structure and large specific surface area [18]. In particular, heteroatom-doped carbon materials based on the zeolitic imidazole framework (ZIF-67) have been extensively investigated in Li–S batteries. The N-doping carbon materials provide high adsorption capacity to LiPSs, and the cobalt nanoparticles promote the redox kinetics of PSs and improve the utilization of the active sulfur content [19]. In another study, the Co–Nx active sites derived from carbonization of Zn/Co-ZIF [20], when used as a separator interlayer, demonstrate good electrocatalytic activity towards the redox reaction of Li$_2$PSs and a 31% increase in capacity. Searching for excellent sulfur-hosting carbon materials and electrocatalysts towards the redox reaction of Li$_2$PSs is central to the community of Li–S batteries.

Additionally, engineering of the morphology and phase of the carbon and metal nanomaterials has been demonstrated to be effective in regulating electrochemical performance. For instance, the amorphous transition metal nanomaterials, which are featured via short-range ordering and anisotropy, have been demonstrated as superior to their crystalline counterparts' electrocatalytic water splitting, etc. [21,22]. The reactions involved in morphology, phase and surface and interface engineering are very complicated, and how the carbon materials and metal species interact with each other remains elusive and challenging to understand.

Herein, a composite composed of worm-like N-doped intertwined porous carbon tubes and Co nanoparticles with low crystallinity (a-Co-NC@C) was prepared by a sequential thermal annealing method, as shown in Scheme 1. Firstly, Zn–Co-ZIF was wrapped by a PAN through a phase inversion method, which was further carbonized in Ar/H$_2$ atmosphere at 950 °C, resulting in the formation of high-crystalline Co nanoparticles supported on carbon materials. Further annealing in ammonia atmosphere at 350 °C results in the growth of intertwined porous carbon nanotubes with large surface area, possibly benefiting from the catalytic effect of Co nanoparticles, and also their reduced crystallinity. Due to the synergy of the uniformly distributed worm-like porous carbon nanotubes and the heavily N-doped low-crystalline cobalt nanoparticles, a-Co-NC@C delivers a superior performance, with a capability of 572 mAh g^{-1} at a current of 3 C and a capacity of 559 mAh g^{-1} after 500 cycles at a current density of 1 C. Even at a high sulfur loading of 3.95 mg cm^{-2}, a specific capacity of 564.1 mAh g^{-1} remains after 200 cycles at 0.1 C.
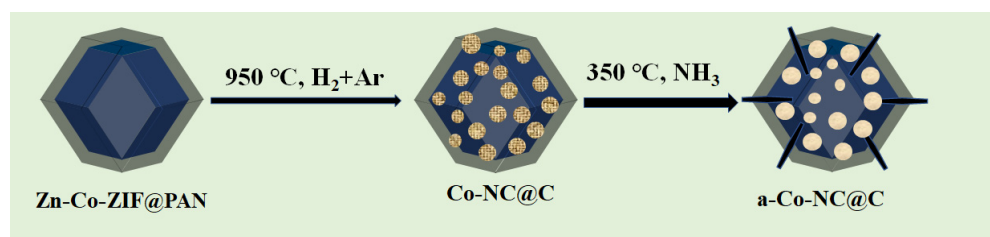
Scheme 1. Illustration of the synthetic process of low-crystalline N-doped porous carbon supported Co nanoparticles.

2. Results

The crystalline structure and polyhedron morphology of Zn–Co-ZIF was examined by XRD (Figure S1) and SEM (Figure S2). The XRD patterns of Zn–Co-ZIF are consistent with those of ZIF-8 and ZIF-67, indicating the successful preparation of Zn–Co-ZIF. The clear sharp peaks in XRD indicates the high crystallinity of Zn–Co-ZIF. The morphology of Co-NC@C and a-Co-NC@C nanocomposites is characterized by SEM and TEM. In Figure 1a,d, Co-NC@C displays a smoother surface and denser structure, and a-Co-NC@C exhibits a rougher surface and porous structure. In the further magnified image in Figure 1b,e, a more detailed surface morphology can be observed. It can be seen that Co-NC@C was covered by finer nanoparticles, which are densely packed together. In contrast, a-Co-NC@C shows a worm-like structure, which consists of carbon nanotubes grown during thermal annealing in ammonia atmosphere under the catalysis of Co nanoparticles.
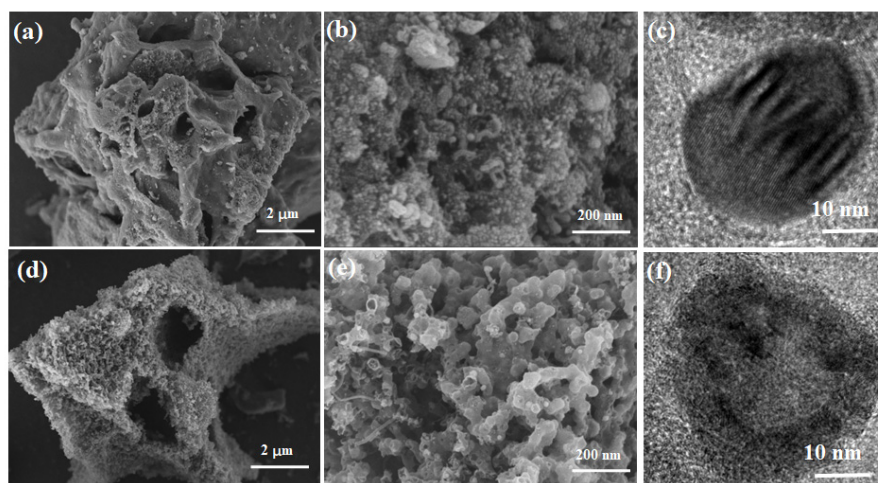

Figure 1. SEM images of at low magnification (**a**); high magnification (**b**) and high-resolution TEM (**c**) for Co-NC@C; SEM images of at low magnification (**d**); high magnification (**e**) and high-resolution TEM (**f**) for a-Co-NC@C.

It can be seen that thermal annealing at 950 °C causes the carbonization of Zn–Co-ZIF@PAN and the formation of a porous carbon-supported Co nanoparticles composite (Co-NC@C). The coating of PAN on Zn–Co-ZIF results in the thorough dispersion and reduced size of the Co nanoparticles on the carbon matrix [23]. Further annealing of Co-NC@C in ammonia atmosphere induces the formation of worm-like heavily N-doped intertwined porous carbon nanotubes in the Co-NC@C composite [24,25]. Such porous carbon nanotubes show high electronic conductivity and a low-weight network for sulfur accommodation [26], and they behave as an excellent electrocatalyst towards the redox reaction of polysulfides [27]. The size of the Co nanoparticles was determined to be 30.6 and 33.3 nm in dimeter for Co-NC@C and a-Co-NC@C, respectively, as shown in Figure 1c,f, which apparently does not change. Usually, such large Co nanoparticles will not show catalytic activity [24,25] towards the growth of carbon nanotubes during thermal annealing in Ar or Ar/H_2 atmosphere. It is speculated that such a strong interaction between Co nanoparticles and ammonia may result in reduced Co nanoparticles and further dissolution of Co species into the adjacent carbon support, which may show good catalytic activity towards the carbon nanotube growth.

The crystallinity of Co nanoparticles after thermal annealing in ammonia atmosphere was monitored by XRD, as shown in Figure 2a. For the Co-NC@C sample, the very sharp diffraction peaks are indexed to Co, indicating the high crystallinity of Co nanoparticles. On the contrary, only very weak and broad diffraction peaks are observed for a-Co-NC@C, indicating the much-reduced crystallinity of Co nanoparticles due to thermal annealing in ammonia atmosphere. This process might be caused by the insertion and subsequent coordination interaction of NH_3 molecules with Co, which disrupts the crystalline structure

of Co nanoparticles, spreading the Co atoms into a larger space and thus reducing the crystallinity of Co nanoparticles. Thermal annealing in ammonia atmosphere may further change the graphitization degree, porosity and N-doping level. As shown in Figure 2b, the D (defect) and G (graphite) bands are observed at 1340 and 1590 cm^{-1}, respectively [28]. The intensity ratio of D to G (I_D/I_G) is similar for Co-NC@C and a-Co-NC@C. However, much high noise was observed for a-Co-NC@C, possibly induced by the high doping content of nitrogen into carbon in Co-NC@C [29].
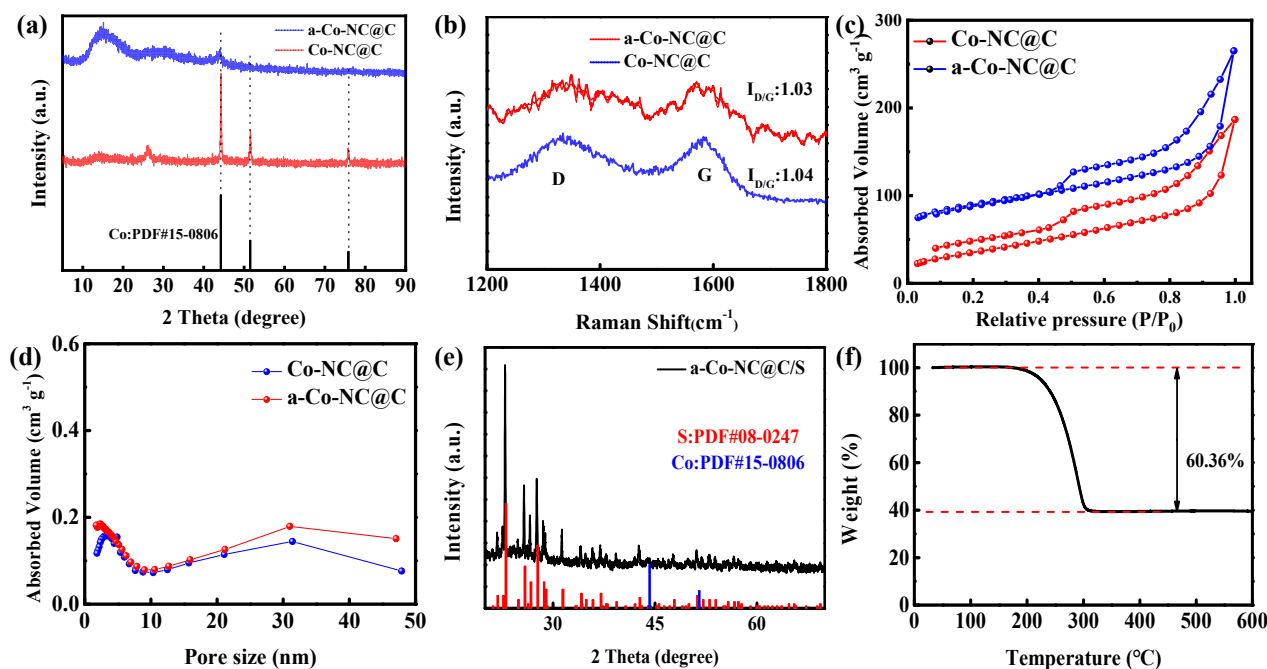

Figure 2. (**a**) XRD, (**b**) Raman spectra, (**c**) nitrogen adsorption/desorption isotherm and (**d**) pore size distributions of Co-NC@C and a-Co-NC@C, respectively. (**e**) XRD pattern and (**f**) TGA of a-Co-NC@C/S.

The porosity of Co-NC@C and a-Co-NC@C is characterized by nitrogen adsorption/desorption isotherms, as shown in Figure 2c,d. The a-Co-NC@C composite shows a surface area of 291.77 m^2 g^{-1} and a pore volume of 0.411 cm^3 g^{-1}, which is much higher than those of the Co-NC@C composite (131.45 m^2 g^{-1} and 0.289 cm^3 g^{-1}), indicating remarkably enhanced surface area and pore volume by thermal annealing in ammonia atmosphere, which offers a large surface area for electrochemical reaction and is also beneficial to the penetration of the electrolyte and mass transfer [30]. Moreover, the pore size of a-Co-NC@C and Co-NC@C is distributed around 1–7 nm and 30 nm, indicating a mesoporous structure of the carbon matrix. When a-Co-NC@C is loaded with sulfur, a-Co-NC@C/S exhibits clear diffraction peaks of sulfur in XRD spectra (Figure 2e), with a sulfur loading of approximately 60 wt%, as revealed by TGA (Figure 2f).

The chemical content of carbon, nitrogen and Co in Co-NC@C and a-Co-NC@C is explored by X-ray photoelectron spectroscopy (XPS). As shown in Figure S3, the fitted C 1*s* spectrum can be deconvoluted into three peaks which, at 284.8 eV, 285.8 eV and 287.6 eV, respectively, can be ascribed to sp^2 carbon, C=N bonds and C–N species. The surface sites of the N-doped carbon can be used as a conductive Lewis base catalyst to improve the adsorption of PSs [31]. Figure 3a shows the high-resolution spectrum of N 1*s*, which can be deconvoluted into a pyridinic N at 398.5 eV and a graphitic N peak at 401.14 ev [32]. It is observed that the content of graphitic N decreases and the content of pyridinic N increases for a-Co-NC@C. In addition, the N content has been increased from 3.62 at% to 4.57 at%. The ability of pyridinic N to introduce strong elements near the Fermi energy level to give electronic states has been reported to change the reaction site and

increase the adsorption on PSs [33]. Therefore, increasing the content of the pyridinic N of a-Co-NC@C can improve the anchoring and catalytic capacity of the LiPSs by increasing the immobilization and catalytic sites. From the high-resolution XPS spectrum of Co $2p3/2$ in Figure 3b, it is observed that the amount of metallic Co at 778.49 eV in Co-NC@C is higher than that in a-Co-NC@C, while only the Co–N bonding component located at 780.06 eV [34] was observed for a-Co-NC@C, indicating heavily doped N content in Co nanoparticles via thermal annealing in ammonia atmosphere. Such positively charged and low-crystalline N-doped Co nanoparticles may provide enhanced interactions with the PSs through both Co–S and Li–N bonds concurrently [35], thus suppressing the shuttle effect [36].
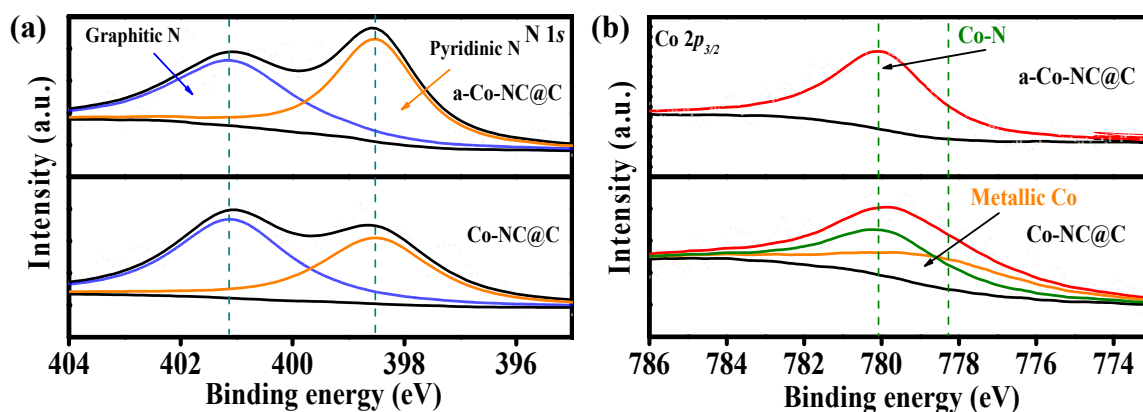

Figure 3. High-resolution XPS spectrum of (**a**) N $1s$ and (**b**) Co $2p_{3/2}$ for Co-NC@C and a-Co-NC@C.

The electrochemical performances of Co-NC@C/S and Co-NC@C-N/S as cathodes of Li–S batteries are shown in Figure 4. The cyclic voltammetry (CV) profiles are shown in Figure 4a. The reduction peaks A and B correspond to the conversion of solid S_8 to long-chain PSs and of short-chain PSs to Li_2S/Li_2S_2, respectively. The oxidation peaks C and D correspond to the conversion of Li_2S/Li_2S_2 to short-chain PSs and, further, to long-chain PSs as well as S_8, respectively [37–39]. It is observed that the current density on the a-Co-NC@C composite is 1.5~2 times that of Co-NC@C, and the polarization voltage between peak A and C is lower than that of Co-NC@C (0.270 vs. 0.354 V) (Table S1), which indicates the evidently enhanced redox kinetics of PSs on a-Co-NC@C composite. Figure 4b shows the rate performance, where a-Co-NC@C displays a capacity of 651 and 572 mAh g^{-1} 2 C and 3 C, much higher than that of Co-NC@C (514 and 342 mAh g^{-1}) [40,41]. The polarization voltage at different current densities of a-Co-NC@C from rate curves (Figure S4) is smaller than that of Co-NC@C, as shown in Figure 4c. This indicates that a-Co-NC@C/S exhibits higher redox kinetics of PSs than Co-NC@C [42]. The high redox kinetics and holding capacity of a-Co-NC@C compared to Co-NC@C may induce an improved cycling performance. As shown in Figure 4d, a-Co-NC@C, as a cathode of Li–S batteries, delivers a specific capacity of 559 mAh g^{-1} after 500 cycles at 1 C and a decay rate of 0.066% per cycle, which is superior to those of the Co-NC@C composite (a capacity of 371 mAh g^{-1} after 500 cycles at 1 C and decay rate of 0.11%). The long cycling performance of a-Co-NC@C/S as a cathode of the Li–S battery was tested at 2 C and 3 C, respectively (as shown in Figure S5), which still exhibits a specific capacity of 509 mAh g^{-1} 500 after cycles at 2 C, and a capacity of 393 mAh g^{-1} after 800 cycles at 2 C.

GITT tests were further performed for Li–S batteries in the first charge and discharge cycle, as shown in Figure 5a for Co-NC@C and Figure 5b for a-Co-NC@C electrodes, respectively, from which the reaction resistance was derived (Figure 5c,d). It is observed from the reaction that the resistance of a-Co-NC@C during discharging is apparently smaller than that of the Co-NC@C electrode, which indicates faster redox kinetics and lithium-ion diffusion on the former than on the latter [39].
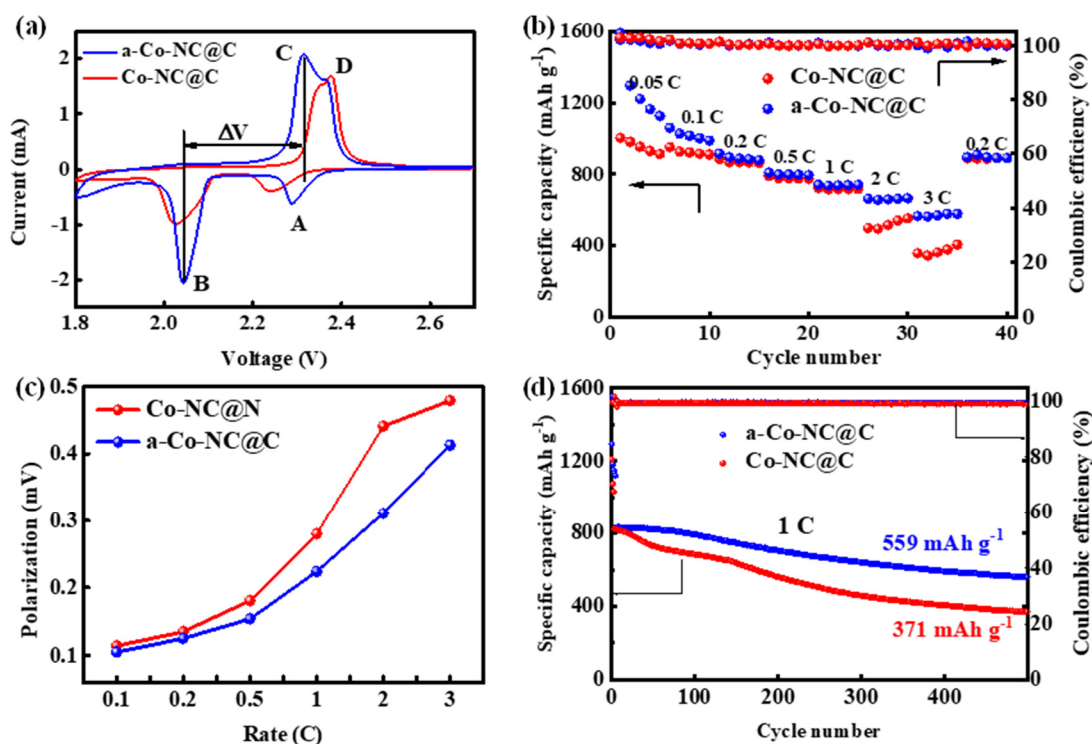
Figure 4. (**a**) CV curves; (**b**) rate performance; (**c**) polarization voltages at different current densities; (**d**) cycling performance at 1 C of Li–S batteries with Co-NC@C/S and a-Co-NC@C/S as cathodes, respectively. The arrows indicate the related axis for the plot in the panels.
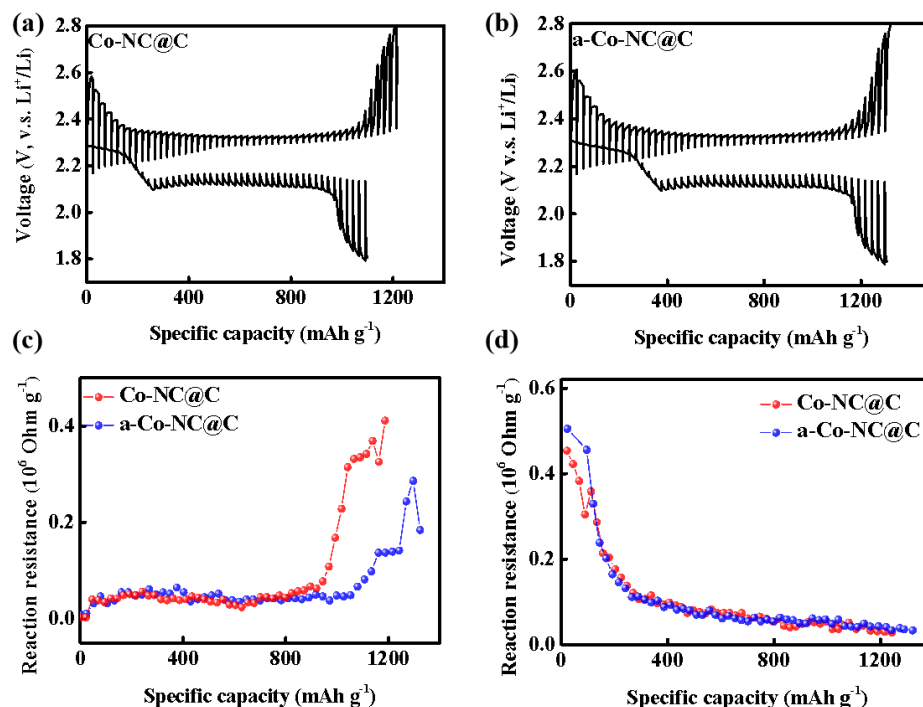
Figure 5. GITT voltage profiles of (**a**) Co-NC@C, (**b**) a-Co-NC@C in the 1st cycle; the reaction resistance of Co-NC@C and a-Co-NC@C in the (**c**) discharging process and (**d**) charging process derived from (**a**,**b**).

The commercialization of Li–S batteries requires high sulfur loading for high capacity and energy density [39,40]. As shown in Figure 6a, at a sulfur loading of 3.95 mg cm^{-2},

an initial capacity of 1071 mAh g^{-1} at the first cycle and a starting discharge capacity of 737.7 mAh g^{-1} after activation at 0.05 C was achieved. The capacity remains at 564.1 mAh g^{-1} after 200 cycles at 0.1 C. At a lower sulfur loading of 2.29 mg cm^{-2}, the starting discharge capacity after activation at 0.05 C was 973.5 mAh g^{-1} and a capacity of 642.8 mAh g^{-1} was achieved after 200 cycles at a current of 0.2 C (Figure 6b). The rate performance of a-Co-NC@C composite at 2 mg cm^{-2} was shown in Figure 6c, which display a capacity of 813, 669, 583, 534, 478 and 428 mAh g^{-1} at 0.1, 0.2, 0.5, 1, 2 and 3 C, respectively, indicating good rate performance for the a-Co-NC@C composite at a high sulfur loading. The a-Co-NC@C composite also showed superior long-cycling performance at high sulfur loading. As shown in Figure 6d, at a load of 2.55 mg cm^{-2}, a capacity of 945 mAh g^{-1} after activation and a capacity of 579 mAh g^{-1} after 400 cycles at 1 C were achieved, corresponding to a capacity decay rate of 0.097% per cycle.
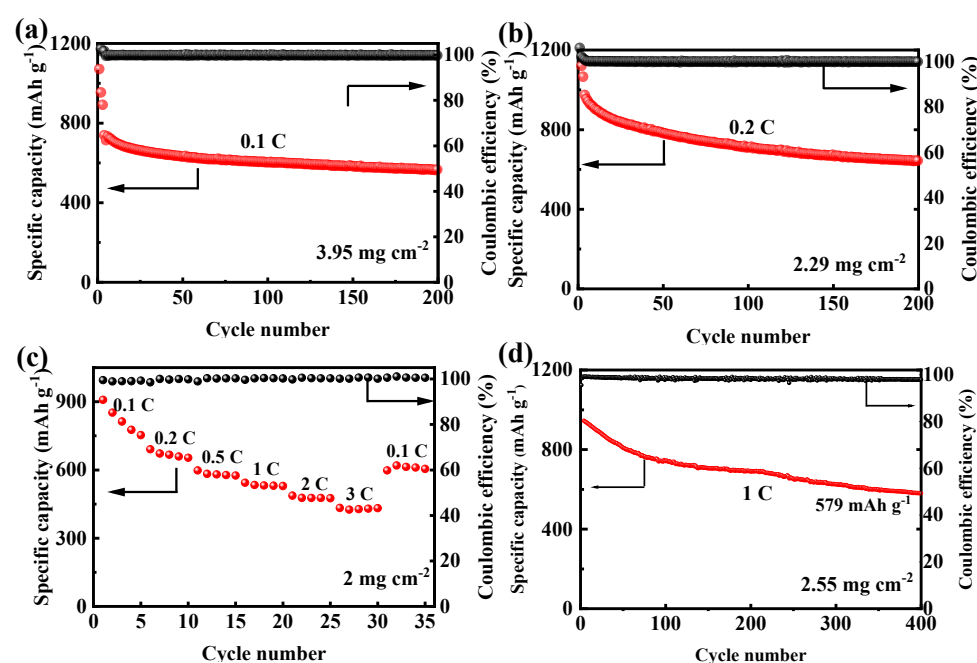
Figure 6. The performance of a-Co-NC@C cathode at high sulfur loading: (**a**) cycling performance at 0.1 C for a sulfur loading of 3.95 mg cm^{-2}; (**b**) cycling performance at 0.2 C at a sulfur loading of 2.29 mg cm^{-2}; (**c**) rate performance at a sulfur loading of 2 mg cm^{-2}; (**d**) cycling performance at 1 C at a sulfur loading of 2.55 mg cm^{-2}. The arrows indicate the related axis for the plot in the panels.

3. Materials and Methods

3.1. Materials

Co(NO$_3$)$_2$·6H$_2$O, Zn(NO$_3$)$_2$·6H$_2$O, 2-methylimidazole (2-MeIM), methanol, N,N-Dimethylformamide (DMF) and polyacrylonitrile (PAN, MW = 150,000) was obtained from Shanghai Macklin Biochemical Co., Ltd., Shanghai, China. All materials have not been further purified before use.

3.1.1. Synthesis of Zn–Co-ZIF and Zn–Co-ZIF@PAN

Typically, 20 mmol of Co(NO$_3$)$_2$·6H$_2$O, 20 mmol of Zn(NO$_3$)$_2$·6H$_2$O and 80 mmol 2-methylimidazole (molar ratio of Co^{2+} to Zn^{2+} is 1:1) were added in a beaker containing 500 mL anhydrous methanol and stirred for 1 h. The solution was centrifuged at a rate of 8000× *g* r min^{-1} for 24 h, and the precipitate was collected, washed three times with methanol and desiccated in an oven at 60 °C for 12 h. The collected purple product was named Zn–Co-ZIF.

A total of 0.5 g Zn–Co-ZIF powder was added into 15 mL DMF and dispersed by ultrasonication for 1 h, into which 0.5 g PAN was then added into and stirred for 4 h. The resulting mixture was dripped into 500 mL of deionized water using a syringe to obtain

a flake product, which was collected by filtration, washed several times with deionized water and desiccated overnight in an oven at 60 °C. The obtained sample is denoted as Zn–Co-ZIF@PAN.

3.1.2. Preparation of Co-NC@C and a-Co-NC@C

Co-NC@C nanocomposites were prepared by thermal annealing Zn–Co-ZIF@PAN powder at 950 °C for 3 h under $Ar/H_2(10\%)$. Co-NC@C was further annealed at 350 °C for 3 h in an ammonia atmosphere to obtain a-Co-NC@C.

3.1.3. Sulfur Loading to Co-NC@C and a-Co-NC@C

Co-NC@C (or a-Co-NC@C) and sulfur powder were ground at a mass ratio of 3:7 for 30 min to achieve a homogeneous mixture, which was then placed in a tube furnace under an Ar atmosphere and annealed at 155 °C for 12 h and then heated to 200 °C for 2 h to remove the excess sulfur. The resulting samples are named Co-NC@C/S and a-Co-NC@C/S, respectively.

3.2. Electrochemical Measurements

Cyclic voltammetry (CV) tests were carried out on an electrochemical workstation CHI 750E with a scan rate of 0.1 mV s^{-1} and an operating voltage window of 1.8–2.7 V. The electrochemical impedance spectroscopy (EIS) was carried out on the CHI 750E in the frequency range 0.01 to 100,000 Hz. Electrochemical performance tests such as long cycling performance, rate performance and charge/discharge curves were carried out on the LAND electric test system.

3.3. The Assembly of Batteries

To load sulfur into Co-CN (or a-Co-CN), Co-CN (or a-Co-CN) was mixed with sulfur powder by grinding for 30 min, transferred into an ampoule and thermally annealed at 155 °C for 12 h with a ramp rate of 2 °C min^{-1} and then 200 °C for another 2 h to obtain Co-NC@C/S (a-Co-NC@C/S). To prepare an active electrode, a slurry was prepared in advance by dispersing Co-CN (or a-Co-CN), super P and PVDF in a mass ratio of 8:1:1 into NMP in a beaker, which was then coated on an Al foil and dried in an oven at 60 °C for 24 h. Battery assembly was carried out in the glove box. The button cell was type CR2016. The cathode material was the Co-NC@C/S and a-Co-NC@C/S obtained above, the anode electrode was lithium metal flake, the separator was a Celgard 2400 and the main component of the electrolyte was LiTFSI dissolved in a 1:1 volume ratio DOL/DME (1, 3-dioxolane = DOL; dimethyl ether = DME) mixture, to which 0.2 M $LiNO_3$ was added. The sulfur loading of the cathode was about 1.2–1.5 mg cm^{-2}, and the ratio of the electrolyte to the sulfur content on the cathode was 25 mL g^{-1}.

4. Conclusions

In this work, we reported the preparation of heavily N-doped worm-like porous carbon nanotube structure mixed low-crystalline Co nanoparticles by sequential thermal annealing of ZnCo-ZIF in $Ar+H_2$ and ammonia atmosphere. The porous carbon was heavily doped with pyridinic N content, and the Co species were completely converted to N-bonded. The formation of porous carbon nanotube structure was ascribed to the catalytic effect of Co nanoparticles endowed by N-doping and reduced crystallinity, which facilitates the adsorption and redox kinetics of LiPSs. Therefore, the a-Co-NC@C/S composite, as sulfur host of the cathode, delivers a specific capacity of 559 mAh g^{-1} after 500 cycles at 1 C and a specific capacity of 572 mAh g^{-1} at 3 C. At a high sulfur loading of 2.55 mg cm^{-2}, it achieves a specific capacity of 579 mAh g^{-1} after 400 cycles at 1 C. Under 2 C and 3 C, it is able to cycle up to 500 and 800 cycles, respectively, and still releases a capacity of 509 and 391 mAh g^{-1}, respectively. This work highlights the importance of the low crystallinity of Co nanoparticles in improving the redox kinetics of LiPSs in LiSB.

Supplementary Materials: The following supporting information can be downloaded at https://www.mdpi.com/article/10.3390/inorganics11070305/s1: Figure S1: XRD pattern of Zn–Co-ZIF; Figure S2: SEM of Zn–Co-ZIF; Figure S3: High resolution XPS spectra of C 1*s* of Co-NC, Co-NC@C and a-Co-NC@C; Figure S4: Charge/discharge profiles at various rates of the cell with cathode of Co-NC@C and a-Co-NC@C; Figure S5: Long term cycling performance at 1 C, 2 C of a-Co-NC@C/S electrode. Table S1: Current density values at different redox peaks and polarization voltages of composite cathodes of Co-NC@C and a-Co-NC@C.

Author Contributions: Conceptualization, J.L. and X.K.; methodology, J.L. and X.K.; validation, H.L., G.L., W.S., K.J. and H.X.; formal analysis, Q.T., K.J. and J.L.; investigation, Q.T. and J.L.; resources, Q.T.; data curation, Q.T. and J.L.; writing—original draft preparation, Q.T. and J.L.; writing—review and editing, Q.T. and X.K.; supervision, X.K.; funding acquisition, X.K. All authors have read and agreed to the published version of the manuscript.

Data Availability Statement: The data presented in this study are available on request from the corresponding author.

Conflicts of Interest: The authors declare no conflict of interest. The funders had no role in the design of the study.

References

1. Wu, Q.; Zhou, X.; Xu, J.; Cao, F.; Li, C. Carbon-Based Derivatives from Metal-Organic Frameworks as Cathode Hosts for Li–S batteries. *J. Energy Chem.* **2019**, *38*, 94–113. [CrossRef]
2. Yu, S.; Cai, W.; Chen, L.; Song, L.; Song, Y. Recent Advances of Metal Phosphides for Li–S Chemistry. *J. Energy Chem.* **2021**, *55*, 533–548. [CrossRef]
3. Xu, R.; Lu, J.; Amine, K. Progress in Mechanistic Understanding and Characterization Techniques of Li-S Batteries. *Adv. Energy Mater.* **2015**, *5*, 1500408. [CrossRef]
4. Jamesh, M.-I. Recent advances on flexible electrodes for Na-ion batteries and Li–S batteries. *J. Energy Chem.* **2019**, *32*, 15–44. [CrossRef]
5. Tong, Z.; Huang, L.; Lei, W.; Zhang, H.; Zhang, S. Carbon-containing Electrospun Nanofibers for Lithium–Sulfur Battery: Current status and future directions. *J. Energy Chem.* **2021**, *54*, 254–273. [CrossRef]
6. Chen, J.; Dong, Q. Research Progress of Key Components in Lithium-Sulfur Batteries. *J. Electrochem.* **2020**, *26*, 648–662. [CrossRef]
7. Seh, Z.W.; Sun, Y.; Zhang, Q.; Cui, Y. Designing High-energy Lithium-Sulfur Batteries. *Chem. Soc. Rev.* **2016**, *45*, 5605–5634. [CrossRef] [PubMed]
8. Zhao, G.; Ahmed, W.H.Z.; Zhu, F. Nitrogen-Sulfur Co-Doped Porous Carbon Preparation and Its Application in Lithium-Sulfur Batteries. *J. Electrochem.* **2021**, *27*, 614–623. [CrossRef]
9. Kai, W. Preparation and Process Optimization of Cathode Materials for Lithium-Sulfur Batteries. *J. Electrochem.* **2020**, *26*, 825–833. [CrossRef]
10. Manthiram, A.; Fu, Y.; Chung, S.H.; Zu, C.; Su, Y.S. Rechargeable lithium-sulfur batteries. *Chem. Rev.* **2014**, *114*, 11751–11787. [CrossRef]
11. Ali, T.; Yan, C. 2 D Materials for Inhibiting the Shuttle Effect in Advanced Lithium-Sulfur Batteries. *ChemSusChem* **2020**, *13*, 1447–1479. [CrossRef] [PubMed]
12. Wei, Z.; Zhang, N.; Wu, F.; Chen, R. Progress and Prospects on Multifunctional Coating Separators for Lithium-Sulfur Battery. *J. Electrochem.* **2020**, *26*, 716–730. [CrossRef]
13. Chen, Y.; Wang, T.; Tian, H.; Su, D.; Zhang, Q.; Wang, G. Advances in Lithium-Sulfur Batteries: From Academic Research to Commercial Viability. *Adv. Mater.* **2021**, *33*, e2003666. [CrossRef]
14. Chung, S.H.; Manthiram, A. Current Status and Future Prospects of Metal-Sulfur Batteries. *Adv. Mater.* **2019**, *31*, e1901125. [CrossRef]
15. Zhang, S.S. Liquid electrolyte lithium/sulfur battery: Fundamental Chemistry, Problems, and Solutions. *J. Power Sources* **2013**, *231*, 153–162. [CrossRef]
16. Ji, S.; Imtiaz, S.; Sun, D.; Xin, Y.; Li, Q.; Huang, T.; Zhang, Z.; Huang, Y. Coralline-Like N-Doped Hierarchically Porous Carbon Derived from Enteromorpha as a Host Matrix for Lithium-Sulfur Battery. *Chem.—A Eur. J.* **2017**, *23*, 18208–18215. [CrossRef]
17. Xia, Y.; Fang, R.; Xiao, Z.; Huang, H.; Gan, Y.; Yan, R.; Lu, X.; Liang, C.; Zhang, J.; Tao, X.; et al. Confining Sulfur in N-Doped Porous Carbon Microspheres Derived from Microalgaes for Advanced Lithium-Sulfur Batteries. *ACS Appl. Mater. Interfaces* **2017**, *9*, 23782–23791. [CrossRef]
18. Yu, L.; Yu, X.Y.; Lou, X.W.D. The Design and Synthesis of Hollow Micro-/Nanostructures: Present and Future Trends. *Adv. Mater.* **2018**, *30*, e1800939. [CrossRef] [PubMed]

19. Li, Y.-J.; Fan, J.-M.; Zheng, M.-S.; Dong, Q.-F. A Novel Synergistic Composite with Multi-functional Effects for High-Performance Li–S Batteries. *Energy Environ. Sci.* **2016**, *9*, 1998–2004. [CrossRef]

20. Kong, Z.; Liu, Q.; Liu, X.; Wang, Y.; Shen, C.; Zhan, L. Co-Nx bonds as Bifunctional Electrocatalytic Sites to Drive The Reversible Conversion of Lithium Polysulfides for Long Life Lithium Sulfur Batteries. *Appl. Surf. Sci.* **2021**, *546*, 148914. [CrossRef]

21. Zhou, Y.; Fan, H.J. Progress and Challenge of Amorphous Catalysts for Electrochemical Water Splitting. *ACS Mater. Lett.* **2021**, *3*, 136–147. [CrossRef]

22. Anantharaj, S.; Noda, S. Amorphous Catalysts and Electrochemical Water Splitting: An Untold Story of Harmony. *Small* **2020**, *16*, 1905779. [CrossRef]

23. Gao, H.; Ning, S.; Zhou, Y.; Men, S.; Kang, X. Polyacrylonitrile-induced Formation of Core-Shell Carbon Nanocages: Enhanced Redox Kinetics towards Polysulfides by Confined Catalysis in Li-S Batteries. *Chem. Eng. J.* **2021**, *408*, 127323. [CrossRef]

24. Meng, J.; Niu, C.; Xu, L.; Li, J.; Liu, X.; Wang, X.; Wu, Y.; Xu, X.; Chen, W.; Li, Q.; et al. General Oriented Formation of Carbon Nanotubes from Metal–Organic Frameworks. *J. Am. Chem. Soc.* **2017**, *139*, 8212–8221. [CrossRef]

25. Li, R.; Rao, D.; Zhou, J.; Wu, G.; Wang, G.; Zhu, Z.; Han, X.; Sun, R.; Li, H.; Wang, C.; et al. Amorphization-induced Surface Electronic States Modulation of Cobaltous Oxide Nanosheets for Lithium-sulfur Batteries. *Nat. Commun.* **2021**, *12*, 3102. [CrossRef] [PubMed]

26. Zhang, S.; Zeng, X.T.; Xie, H.; Hing, P. A Phenomenological Approach for The Id/Ig Ratio and sp3 Fraction of Magnetron Sputtered a-C Films. *Surf. Coat. Technol.* **2000**, *123*, 256–260. [CrossRef]

27. Li, C.; Sui, X.-L.; Wang, Z.-B.; Wang, Q.; Gu, D.-M. 3D N-doped Graphene Nanomesh Foam for Long Cycle Life Lithium-Sulfur Battery. *Chem. Eng. J.* **2017**, *326*, 265–272. [CrossRef]

28. Wang, J.; Luo, D.; Li, J.; Zhang, Y.; Zhao, Y.; Zhou, G.; Shui, L.; Chen, Z.; Wang, X. "Soft on Rigid" Nanohybrid as The Self-supporting Multifunctional Cathode Electrocatalyst for High-performance Lithium-Polysulfide Batteries. *Nano Energy* **2020**, *78*, 105293. [CrossRef]

29. Chen, J.-J.; Yuan, R.-M.; Feng, J.-M.; Zhang, Q.; Huang, J.-X.; Fu, G.; Zheng, M.-S.; Ren, B.; Dong, Q.-F. Conductive Lewis Base Matrix to Recover the Missing Link of Li2S8 during the Sulfur Redox Cycle in Li–S Battery. *Chem. Mater.* **2015**, *27*, 2048–2055. [CrossRef]

30. Cho, Y.J.; Kim, H.S.; Im, H.; Myung, Y.; Jung, G.B.; Lee, C.W.; Park, J.; Park, M.-H.; Cho, J.; Kang, H.S. Nitrogen-Doped Graphitic Layers Deposited on Silicon Nanowires for Efficient Lithium-Ion Battery Anodes. *J. Phys. Chem. C* **2011**, *115*, 9451–9457. [CrossRef]

31. Yuan, H.; Zhang, W.; Wang, J.-g.; Zhou, G.; Zhuang, Z.; Luo, J.; Huang, H.; Gan, Y.; Liang, C.; Xia, Y.; et al. Facilitation of Sulfur Evolution Reaction by Pyridinic Nitrogen Doped Carbon Nanoflakes for Highly-Stable Lithium-Sulfur Batteries. *Energy Storage Mater.* **2018**, *10*, 1–9. [CrossRef]

32. Luo, M.; Cai, J.; Zou, J.; Jiang, Z.; Wang, G.; Kang, X. Promoted Alkaline Hydrogen Evolution by An N-Doped Pt–Ru Single Atom Alloy. *J. Mater. Chem. A* **2021**, *9*, 14941–14947. [CrossRef]

33. Yao, S.; Xue, S.; Peng, S.; Jing, M.; Qian, X.; Shen, X.; Li, T.; Wang, Y. Synthesis of Graphitic Carbon Nitride at Different Thermal-Pyrolysis Temperature of Urea and Its Application in Lithium–Sulfur Batteries. *J. Mater. Sci.-Mater. Electron.* **2018**, *29*, 17921–17930. [CrossRef]

34. Wang, N.; Xu, Z.; Xu, X.; Liao, T.; Tang, B.; Bai, Z.; Dou, S. Synergistically Enhanced Interfacial Interaction to Polysulfide via N,O Dual-Doped Highly Porous Carbon Microrods for Advanced Lithium–Sulfur Batteries. *ACS Appl. Mater. Interfaces* **2018**, *10*, 13573–13580. [CrossRef]

35. Zhang, B.; Liu, X.; Li, D. Electrochemical Properties of Sulfur in Different Carbon Support Materials. *J. Electrochem.* **2019**, *25*, 749–756. [CrossRef]

36. Wang, J.; Peng, Q.; Guan, Y.; Wang, W.; Wang, A.; Liu, Q.; Huang, Y. Efficient Interface Enabled by Nano-Hydroxyapatite@Porous Carbon for Lithium-Sulfur Batteries. *J. Electrochem.* **2022**, *28*, 2219008. [CrossRef]

37. Ji, X.; Wang, J.Y.; Wang, A.B.; Wang, W.K.; Yao, M.; Huang, Y.Q. Preparation of Highly-Cyclized Sulfurized Polyacrylonitrile for Lithium-Sulfur Batteries. *J. Electrochem.* **2022**, *28*, 2219010. [CrossRef]

38. Li, X.Y.; Zhao, C.X.; Li, B.Q.; Huang, J.Q.; Zhang, Q. Advances on Composite Cathodes for Lithium-Sulfur Batteries. *J. Electrochem.* **2022**, *28*, 2219013. [CrossRef]

39. Gao, H.C.; Ning, S.L.; Lin, J.J.; Kang, X.W. Molecular Perturbation of 2D Organic Modifiers on Porous Carbon Interlayer: Promoted Redox Kinetics of Polysulfides in Lithium-Sulfur Batteries. *Energy Storage Mater.* **2021**, *40*, 312–319. [CrossRef]

40. Gao, H.; Ning, S.; Zou, J.; Men, S.; Zhou, Y.; Wang, X.; Kang, X. The Electrocatalytic Activity of BaTiO₃ Nanoparticles towards Polysulfides Enables High-Performance Lithium–Sulfur Batteries. *J. Energy Chem.* **2020**, *48*, 208–216. [CrossRef]

41. Rana, M.; Ahad, S.A.; Li, M.; Luo, B.; Wang, L.; Gentle, I.; Knibbe, R. Review on Areal Capacities and Long-Term Cycling Performances of Lithium Sulfur Battery at High Sulfur Loading. *Energy Storage Mater.* **2019**, *18*, 289–310. [CrossRef]

42. Peng, J.; Huang, J.; Cheng, X.; Zhang, Q. Review on High-Loading and High-Energy Lithium–Sulfur Batteries. *Adv. Energy Mater.* **2017**, *7*, 1700260. [CrossRef]